Supporting Information

Carrot-Inspired Solar Thermal Evaporator

Yaojia Long[a], Shaolong Huang[a], Huan Yi[a], Jiaqi Chen[a], Jiahao Wu[a], Qiufan Liao[a], Huawei Liang[a], Hongzhi Cui[b], Shuangchen Ruan[a], and Yu-Jia Zeng*[a]*

[a.]Shenzhen Key Laboratory of Laser Engineering, College of Physics and Optoelectronic Engineering, Shenzhen University, Nanhai Boulevard 3688, China. Email: yjzeng@szu.edu.cn; hwliang@szu.edu.cn

[b.]College of Civil Engineering, Shenzhen University, Nanhai Boulevard 3688, China.

COMSOL simulation of temperature distribution in ECB

Considering the water confinement of ECB network and the convection in the micron channels, the heat transfer in ECB could be described by the equation given below:

$$E_{in} = \rho C_p \frac{\partial T(\mathrm{x},t)}{\partial t} + \rho C_p v \cdot \nabla T(\mathrm{x},t) + \nabla[k \nabla T(\mathrm{x},t)]$$

Where the x and t are the space vector and time, respectively; v and k stand for the fluid flow speed and thermal conductivity of the aqueous medium; ρ, Cp, and $T(x, t)$ are the mass density, liquid thermal capacity and the local temperature, respectively; E_{in} represents the thermal energy input from the optical-thermal conversion. According to the previous study, the heat transfer model can be simplified as a semi-infinite medium for the Cartesian coordinate system. The numerical simulations were conducted by COMSOL Multiphysics 4.4, modeling with Laminar Flow and Heat Transfer modules by finite element simulation software. Wherein, a steady and constant heat flux of 100 mW cm^{-2} occurs on the top (Z = 500), corresponding to the solar energy input on the surface of ECB. The material structure can be approximately regarded as repeated hexagonal cellular structure, so the two-dimensional model can be discretized

into a single unit for analysis. The convection heat transfer in the carrot internal microporous network was disabled to describe the water restriction effect. To carry out a qualitative analysis, we assume that the temperature of environment and water was set to 20 ºC (293.15 K). In the heat transfer setting, the velocity calculated by the laminar flow interface was used as the convection velocity of heat transfer. Solid wall as the heat source conditions, the total thermal power equal to 100 mW cm^{-2}. The bottom temperature was set at room temperature 293.15 K. The parameters of common material water were used to calculate the material properties of fluid, and the thermal conductivity of solid was 0.03206 W m^{-1} K^{-1}.The simulation results show that due to the continuous photothermal conversion (heating) and evaporation process (cooling) on the surface, the ECB surface temperature finally reaches a dynamic stability, which is close to the experimental temperature distribution.

COMSOL Simulation of water transport in ECB

The essence of the model we established is that the fluid flows in the porous medium. We approximately regard the porosity of the porous medium as equal and ignore the complexity caused by deformation and channel bending to derive the steady state model of fluid transport in the ECB. The internal microporous network of the carrot and the water fluid in the porous channel will be taken as the penetrable solid and fluid. Meanwhile, the conservation of momentum are depicted by the Navier-Stokes equations shown as follow:

$$\rho \frac{dv}{dt} = -\nabla P + \rho F + \mu \Delta v$$

Where ρ is the fluid density; v and t stand for the fluid flow speed of water phase and time, respectively; P represents the intrinsic fluid pressure, comprising the osmotic

pressure and the remaining part of the intrinsic fluid pressure; F is the body force; μ is the viscosity of the water at room temperature (20 ^{o}C, 1×10^{-3} Pa s). Numerical simulations are conducted by COMSOL Multiphysics 4.4, under the steady analysis mode. The material structure can be approximately regarded as repeated hexagonal cellular structure, so the two-dimensional model can be discretized into a single unit for analysis. In laminar flow setting, surface boundary conditions were given on the flow rate of 4.08 e^{-7} m s^{-1} ($\approx$1.47 kg m^{-2} h^{-1}/1000 kg m^{-3}), the bottom was set as free flow conditions. The solid wall surface was considered to be no slip wall, so the velocity was nearly zero. As a result, the simulation results represent that the center of the ECB microchannel has the highest velocity and the maximum value is 0.6 μm s^{-1}.
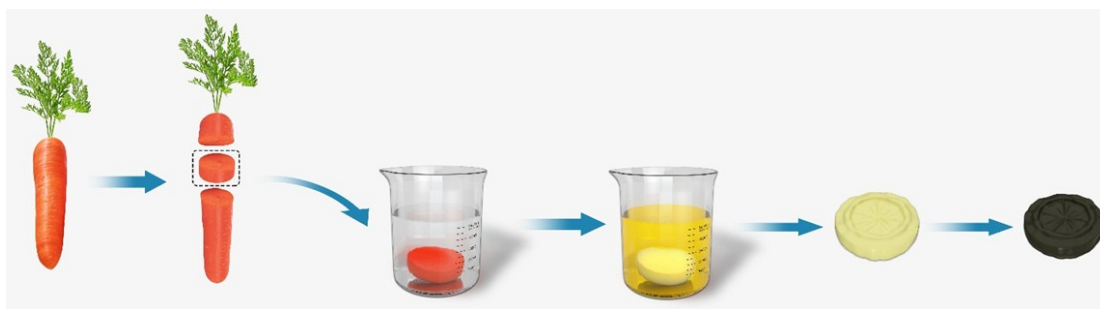
Figure S1. The detailed process for preparing ECB.
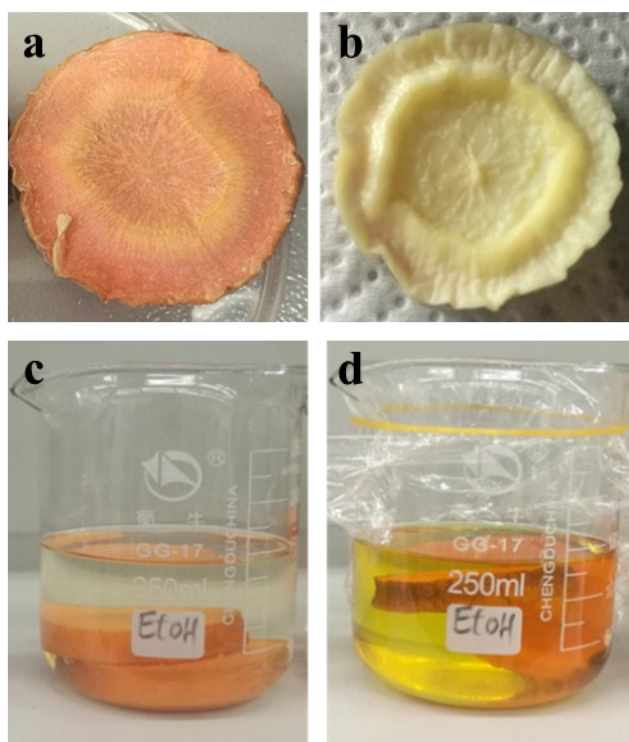
Figure S2. a) Photographs of the a) natural carrot and b) carrot after 4-day dehydration. c)~d) Photos of the ethanol solution in which the carrot is soaked for 2 days. The dissolution of β-carotene and other organics make the solution change from c) colorless to d) yellowish.
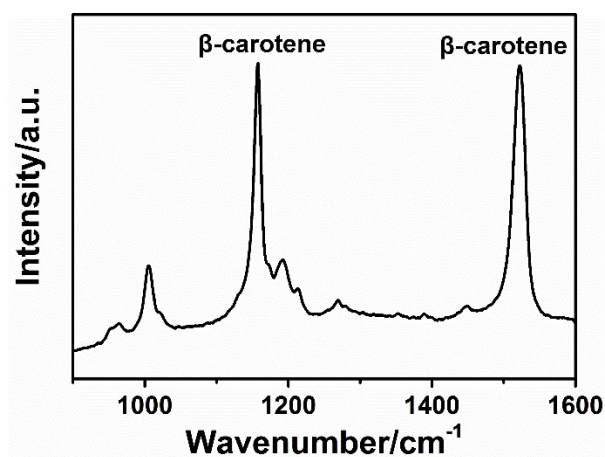
Figure S3. Raman spectra of the ethanol solution in which the carrot is soaked for 2 days.
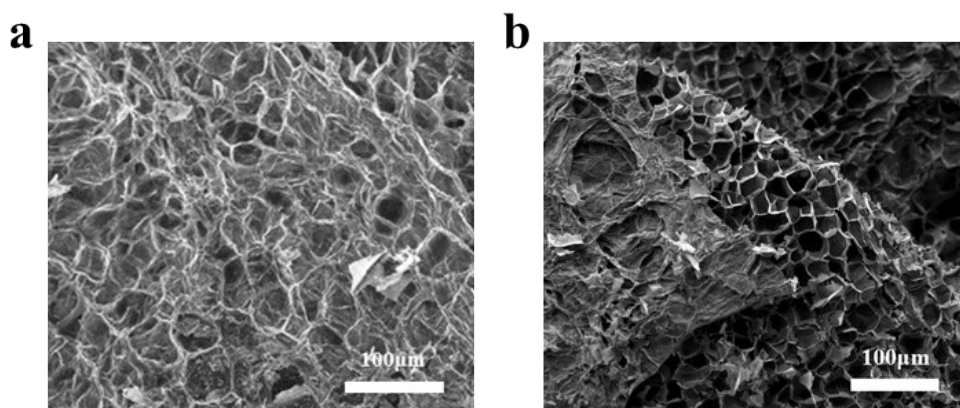
Figure S4. SEM images of the carbonized carrots with the pyrolysis temperature of 550 °C. a) SEM images of the carbonized carrots without the ethanol treatment. b) SEM images of the carbonized carrots with the ethanol treatment.

Figure S5. Photographs of the carbonized carrots. a) The pyrolysis temperature of 300 °C with the ethanol treatment. b) The pyrolysis temperature of 550 °C without the ethanol treatment. c) The pyrolysis temperature of 550 °C with the ethanol treatment.
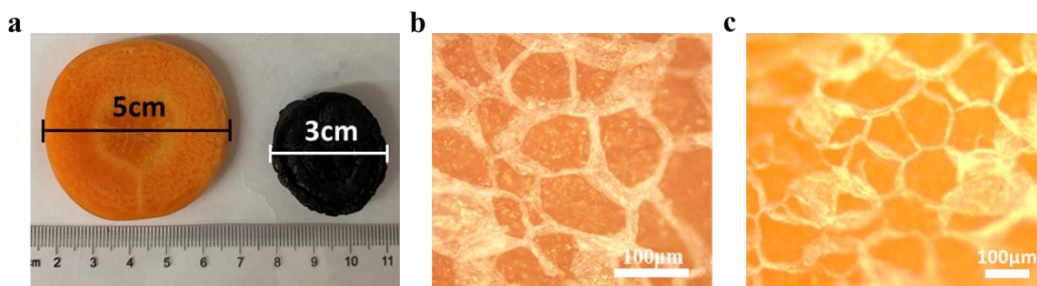
Figure S6. a) The morphology of natural and carbonized carrots. The diameters of two carrots are approximately 5 and 3 cm, respectively b) Optical microscope images of the natural carrot. c) Optical microscope images of the carrot after dehydration.
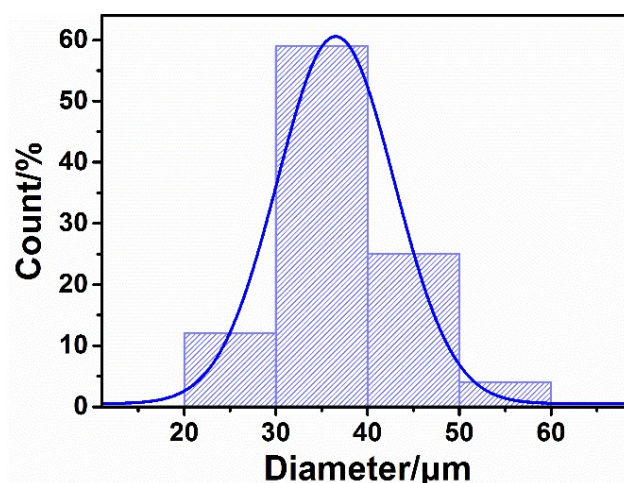
Figure S7. Pore size distributions of the ethanol-treated-carrot biochar. The average pore size is estimated as 37 μm.
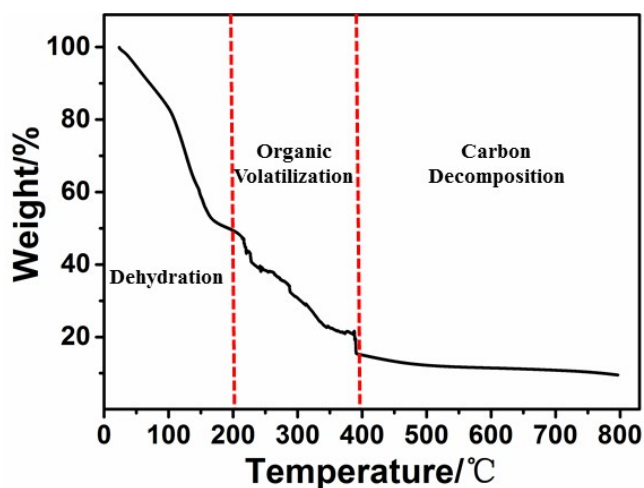
Figure S8. TGA measurements for natural carrots. The red dotted line divides the temperature range into three parts, dehydration, organic volatilization and carbon decomposition (from left to right, respectively).
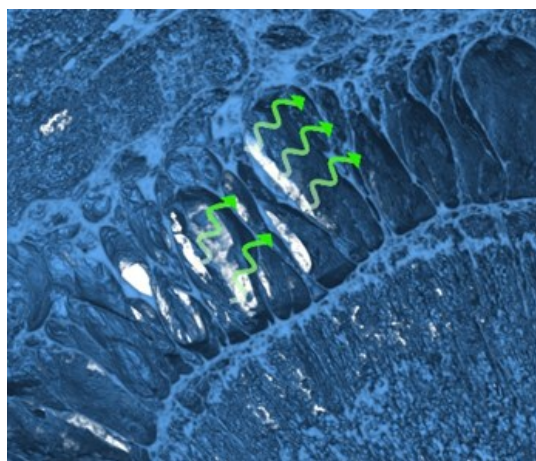
Figure S9. Local structure of ECB reconstructed by X-ray computed Tomography (XCT) technology. The structure that is loose and porous enough to facilitate water transport (green arrow).
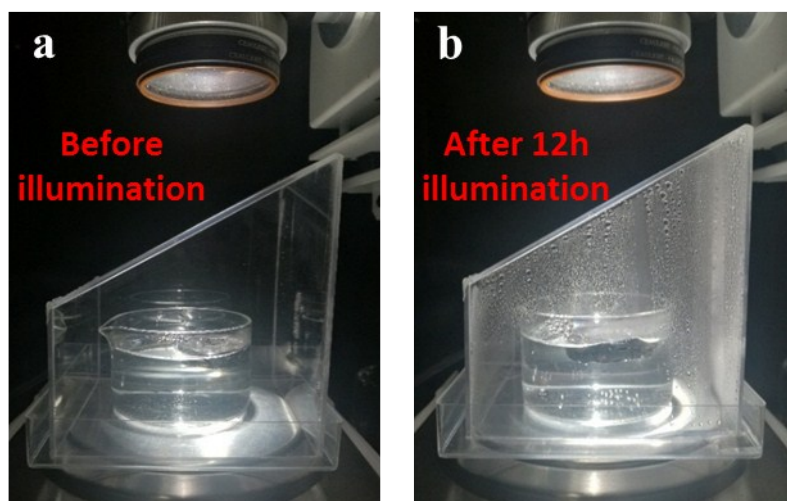
Figure S10. Solar thermal vapor generation device. The performance of vapor generation devices a) before and b) after illumination.
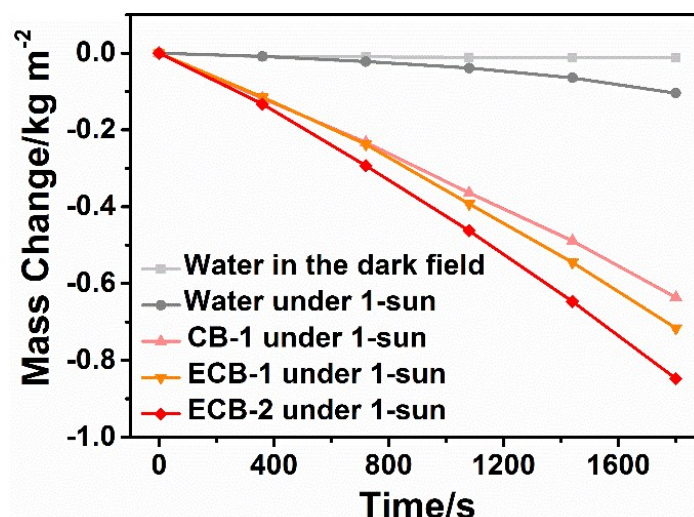
Figure S11. Mass change of water over time in the dark field and under 1-sun illumination. Obviously, the mass change of carrot with ethanol treatment (ECB-1) is higher than the carrot without ethanol treatment (CB-1), and for both ethanol-treated carrots, the one with the heating rate of 5 ^{o}C per minutes (ECB-2) is higher than that with the heating rate of 10 ^{o}C per minutes (ECB-1). The pyrolysis temperature is 550 ^{o}C.
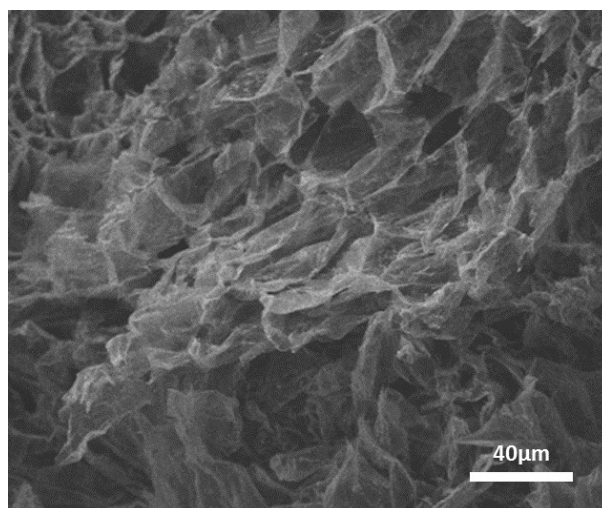
Figure S12. The SEM image of ECB-600.
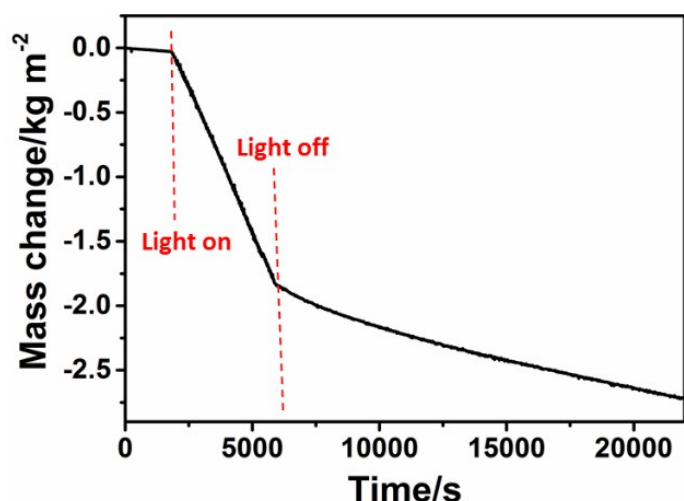
Figure S13. The mass change of the ECB. When the light is on (at the time of 1800 s), the evaporation rate is sharply increased from 0.058 to 1.585 kg m^{-2} h^{-1}, and after 3600s illumination, the light is off, the evaporation rate is quickly decreased to 0.238 kg m^{-2} h^{-1} and keeps steady within 4.7 hours.
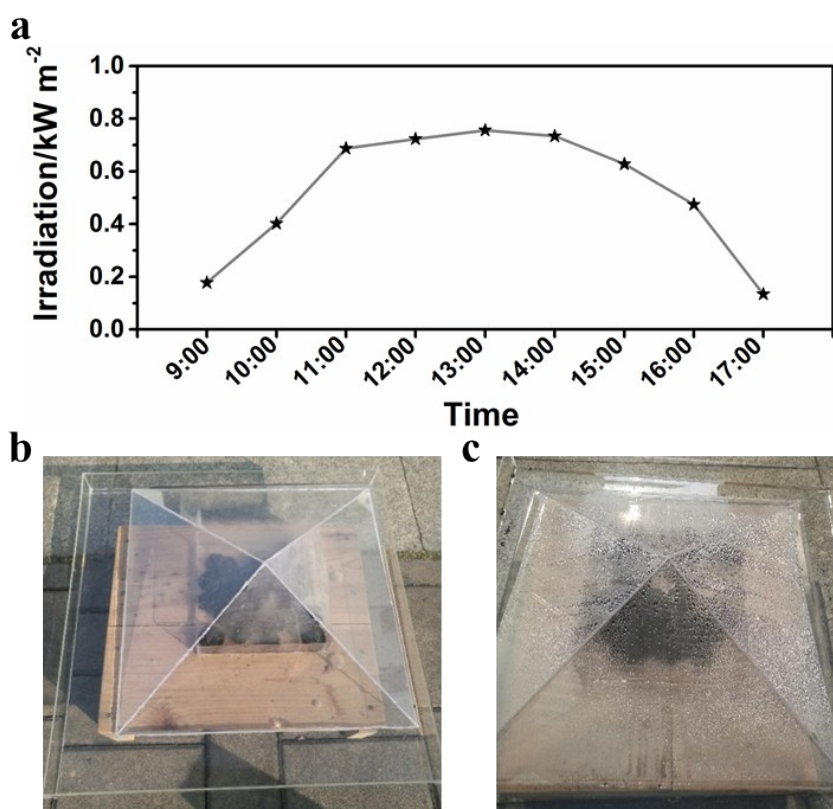
Figure S14. a) The sunlight irradiation of a day. From 9:00 to 17:00 o'clock, with an average heat flux of 0.524 kW m^{-2}. The outdoor experiment of the carrot-based vapor generation device in the natural sunlight. b) The carrots floats on the seawater in a container that is located in an acrylic square holder (2304 cm^2). The vapor is condensed via the transparent condenser and flows to the bottom of the holder, where the purified water is stored. c) After just 1.5 hours, the water droplets are covered over the whole condenser walls.

Table S1. Summary of photothermal materials reported in recent years.

		Materials	Evaporation Rate (kg m^{-2} h^{-1})	References
Carbon	Graphite	GO-based aerogel	1.622	1
		3D graphene (3DG)	2.6	2
		Activated carbon fiber (ACF)	1.22	3
		rGO/PS bi-layered membrane	1.31	4
		Carbon nanotube (CNT)	1.32	5
		Conjugated micro-porous polymers (CMPs)	1.4406	6
		Melamine sponges (MS)	1.98	7
	Biochar	Cotton	1.62	8
		Mushroom	1.475	9
		Wood	1.2	10
		Wood	1.3	11
		Cotton-CuS	1.63	12
		Lotus seedpods	1.3	13
		Carrot	**2.04**	**This work**
Others		Polyacrylonitrile (PAN)	1.3	14
		Polymeric fibrous matrix	1.24	15
		Mixed metal oxide (MMO)	1.93	16
		Cellulose nanofibrils (CNFs)	1.11	17
		p-PEGDA–PANi hydrogel	1.4	18
		(AuNP)/poly(pphenylene benzobisoxazole) nanofibre (PBONF)	1.424	19
		PPy/PVA gels	3.2	20
		Black Ag nanostructures	1.32	21

Supplementary References:

[1] X. Hu, W. Xu, L. Zhou, Y. Tan, Y. Wang, S. Zhu and J. Zhu, *Adv. Mater.* **2017**, 29, 1604031.

[2] Y. Yang, R. Zhao, T. Zhang, K. Zhao, P. Xiao, Y. Ma, P. M. Ajayan, G. Shi and Y. Chen, *ACS Nano* **2018**, 12, 829-835.

[3] H. Li, Y. He, Y. Hu and X. Wang, *ACS appl. Mater. Inter.* **2018**, 10, 9362-9368.

[4] L. Shi, Y. Wang, L. Zhang and P. Wang, *J. Mater. Chem. A* **2017**, 5, 16212-16219.

[5] Y. Wang, L. Zhang and P. Wang, *ACS Sustain. Chem. Eng.* **2016**, 4, 1223-1230.

[6] P. Mu, Z. Zhang, W. Bai, J. He, H. Sun, Z. Zhu, W. Liang and A. Li, *Adv. Energy Mater.* **2019**, 9, 1802158.

[7] F. Gong, H. Li, W. Wang, J. Huang, D. Xia, J. Liao, M. Wu and D. V. Papavassiliou, *Nano Energy* **2019**, 58, 322-330.

[8] X. Li, J. Li, J. Lu, N. Xu, C. Chen, X. Min, B. Zhu, H. Li, L. Zhou, S. Zhu, T. Zhang and J. Zhu, *Joule* **2018**, 2, 1331-1338.

[9] X. Hu, W. Xu, X. Li, L. Zhou, S. Zhu and J. Zhu, *Adv. Mater.* **2017**, 29, 1606762.

[10] T. Li, H. Liu, X. Zhao, G. Chen, J. Dai, G. Pastel, C. Jia, C. Chen, E. Hitz, D. Siddhartha, R. Yang and L. Hu, *Adv. Funct. Mater.* **2018**, 28, 1707134.

[11] Z. Chen, B. Dang, X. Luo, W. Li, J. Li, H. Yu, S. Liu and S. Li, *ACS appl. Mater. Inter.* **2019**, 11, 26032-26037.

[12] X. Wu, M. E. Robson, J. L. Phelps, J. S. Tan, B. Shao, G. Owens and H. Xu, *Nano Energy* **2019**, 56, 708-715.

[13] J. Fang, J. Liu, J. Gu, Q. Liu, W. Zhang, H. Su and D. Zhang, *Chem. Mat.* **2018**, 30, 6217-6221.

[14] W. Xu, X. Hu, S. Zhuang, Y. Wang, X. Li, Z. Lin, S. Zhu and Z. Jia, *Adv. Energy Mater.* **2018**, 1702884.

[15] J. Yong, C. Jian, Y. Shi, S. Le, S. Hong and W. Peng, *J. Mater. Chem. A* **2018**, 6, 7942-7949.

[16] Y. Shi, R. Li, Y. Jin, S. Zhuo, L. Shi, J. Chang, S. Hong, K.-C. Ng and P. Wang, *Joule* **2018**, 2, 1171-1186.

[17] F. Jiang, H. Liu, Y. Li, Y. Kuang, X. Xu, C. Chen, H. Huang, C. Jia, X. Zhao, E. Hitz, Y. Zhou, R. Yang, L. Cui and L. Hu, *ACS appl. Mater. Inter.* **2018**, 10, 1104-1112.

[18] X. Yin, Y. Zhang, Q. Guo, X. Cai, J. Xiao, Z. Ding and J. Yang, *ACS appl. Mater. Inter.* **2018**, 10, 10998-11007.

[19] M. Chen, Y. Wu, W. Song, Y. Mo, X. Lin, Q. He and B. Guo, *Nanoscale* **2018**, 10, 6186-6193.

[20] F. Zhao, X. Zhou, Y. Shi, X. Qian, M. Alexander, X. Zhao, S. Mendez, R. Yang, L. Qu and G. Yu, *Nat. Nanotechnol.* **2018**, 13, 489–495.

[21] J. Chen, J. Feng, Z. Li, P. Xu, X. Wang, W. Yin, M. Wang, X. Ge and Y. Yin, *Nano Lett.* **2019**, 19, 400-407